

Supplemental Information

Stiffening of a Fibrous Matrix after Recovery of Contracted Inclusions

Mainak Sarkar,^{a,*} Mohammad Tanver Hossain,^{b,c} Randy H. Ewoldt,^{b,c,f} Christina Laukaitis,^{a,d,e,h} Amy Wagoner Johnson^{a,b,c,d,g}

^aCarl R. Woese Institute for Genomic Biology, University of Illinois Urbana-Champaign

^bMechanical Science and Engineering, Grainger College of Engineering, University of Illinois Urbana-Champaign

^cBeckman Institute for Advanced Science and Technology, University of Illinois Urbana-Champaign

^dBiomedical and Translational Sciences, Carle Illinois College of Medicine, University of Illinois Urbana-Champaign

^eClinical Sciences, Carle Illinois College of Medicine, University of Illinois Urbana-Champaign

^fMaterials Research Laboratory, University of Illinois Urbana-Champaign

^gCZ Biohub Chicago, LLC, Chicago, Illinois

^hCarle Health, Urbana, Illinois

* Corresponding author: Mainak Sarkar, mainak@illinois.edu

Supplemental Figures

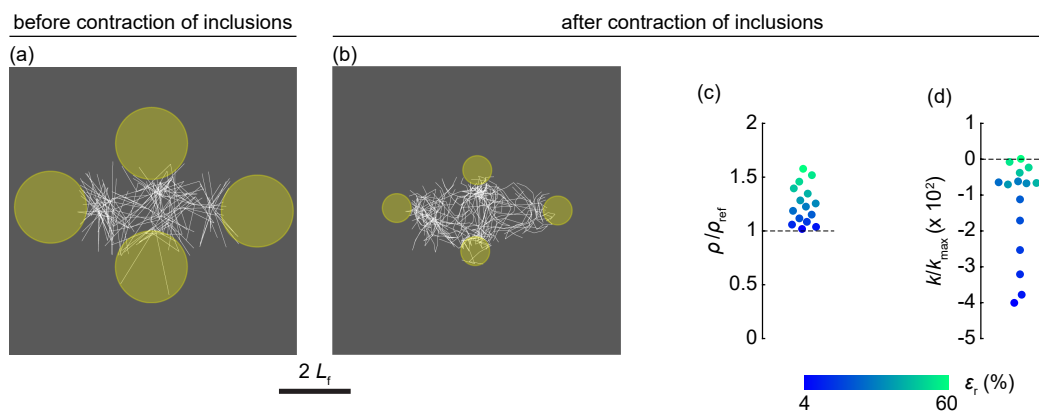


Figure S1. Reproducing established matrix nonlinearity by contracting inclusions. (a, b) Representative matrix region of interest between inclusions before (panel a) and after inclusion contraction by 60% (panel b). (c) Density (ρ) of the matrix region of interest as inclusions contract, normalized by the density of the reference configuration (ρ_{ref}). (d) Incremental bulk stiffness (k) of the region of interest as inclusions contract by varying levels, normalized against the maximal stiffness (k_{max}) at the highest inclusion contraction. The matrix softened, consistent with predictions from prior studies [1, 2]. Data points in panels c and d represent means from seven independent matrices. Background colors in panels a and b are used solely to enhance graphic contrast. Color bar indicates inclusion contraction levels (ϵ_r) for data points in panels c and d.

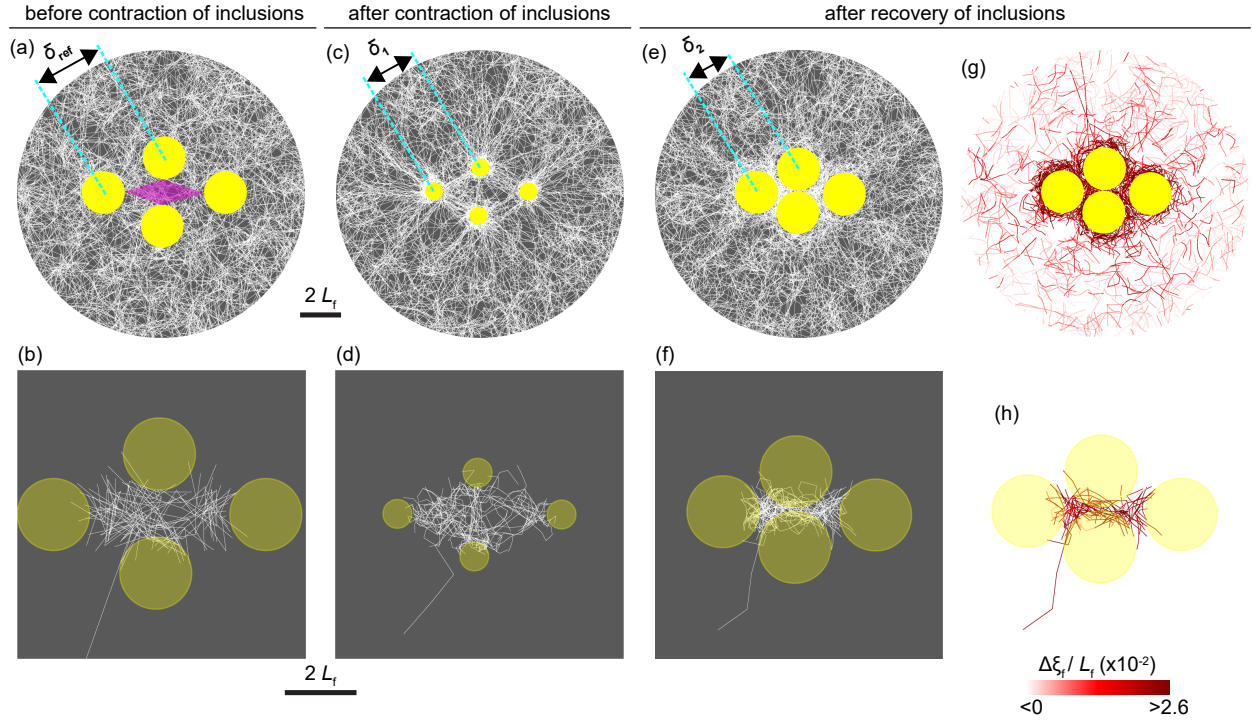


Figure S2. Simulations on another independent matrix with initial inter-inclusion spacings of $\delta_{\text{ref}} \approx 3.5L_f$ (panels a, b) demonstrate the process of matrix remodeling as inclusions contract by 60% (panels c, d) and recover (panels e, f). Defects induced in fibers during the recovery process are color-coded by the extent of defect (excess length) induced in fibers ($\Delta\xi_r$; color bar) and shown in panels g and h. The region of interest between inclusions displayed in panels b, d, f, and h corresponds to panels a, c, e, and g, respectively.

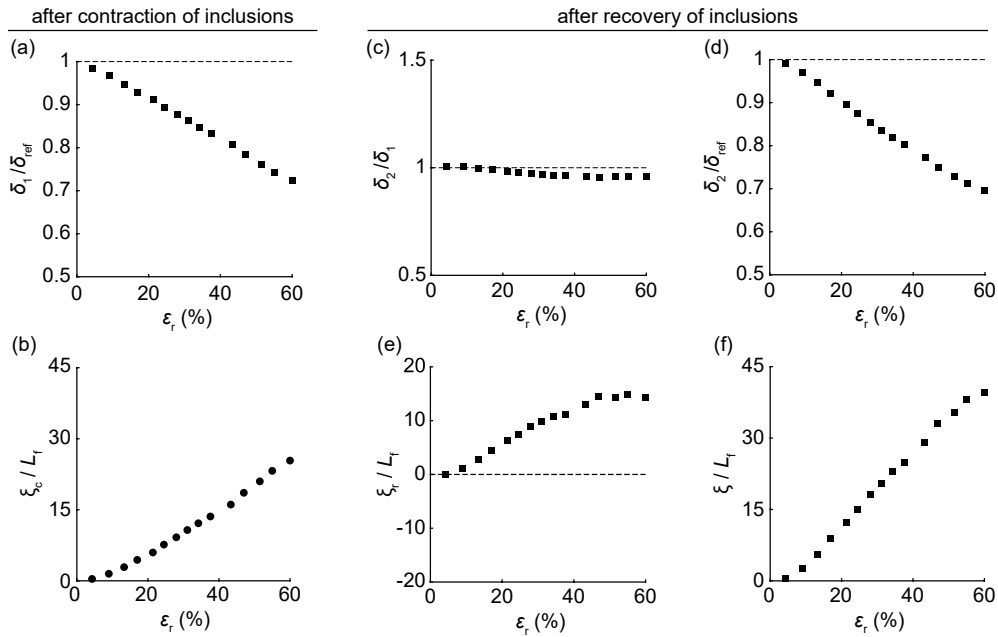


Figure S3. Alternative representation of parameters plotted against ϵ_r on the abscissa for Fig. 2e (panel a), Fig. 2f (panel b), Fig. 3e (panel c), Fig. 3f (panel d), Fig. 3g (panel e), and Fig. 3h (panel f).

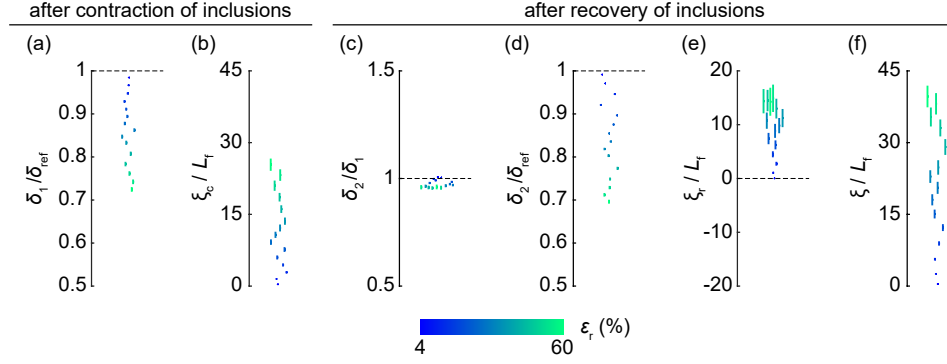


Figure S4. Data spread across means for the data points shown in Fig. 2e (panel a), Fig. 2f (panel b), Fig. 3e (panel c), Fig. 3f (panel d), Fig. 3g (panel e), and Fig. 3h (panel f). In all panels, vertical bar lengths represent twice the standard error, with the center of each bar indicating the mean calculated from seven independent matrices. Color bar denotes inclusion contraction levels for the data points across all panels.

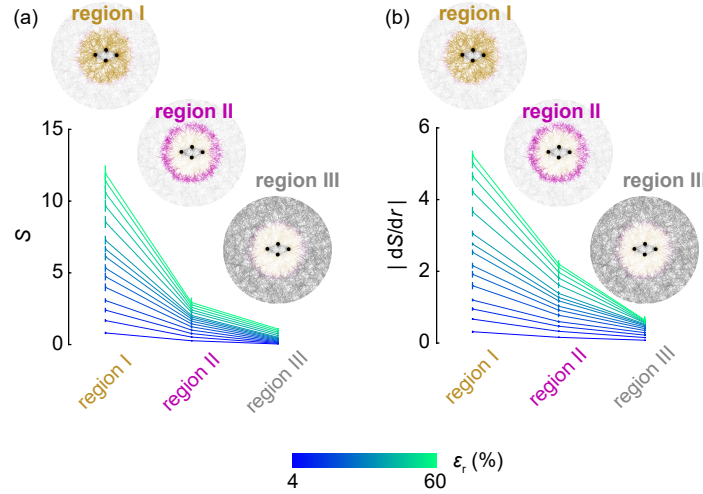


Figure S5. Strain-induced fiber alignment, radial relative to the geometric center of the cluster, surrounding the contracted cluster. (a) The order parameter S quantifies radial fiber alignment, showing a high degree of alignment in region I immediately surrounding the cluster, which drops by $> 70\%$ in region II and by $> 90\%$ in region III. Insets highlight the regions. (b) Normalized microstructural gradient, $|dS/dr|$, calculated in regions I, II, and III (insets) surrounding the cluster, for different levels of inclusion contraction. Region I (yellow), immediately surrounding the cluster, spanned $r \approx 2.5L_f$ to $r \approx 5.5L_f$ from the cluster center and exhibited a pronounced gradient, indicating a sharp reduction in radial fiber alignment radially outward from the cluster. Region III (grey), farther from the cluster, spanned $r \approx 6L_f$ to $r \approx 11L_f$ and showed a negligibly small gradient across this range. Microstructural gradient in the region I immediately surrounding the contracted cluster is depicted in Fig. 4b of the manuscript. Error bars indicate the standard error of the mean from seven independent matrices. Color bar denotes inclusion contraction levels.

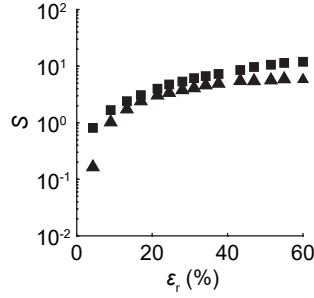


Figure S6. The relative radial alignment of fibers (S) immediately surrounding the recovered cluster (\blacktriangle) exhibits a slight loss of alignment across all levels of ϵ_r compared to the contracted state (\blacksquare). This provides evidence of fiber buckling and postbuckling near the recovered cluster.

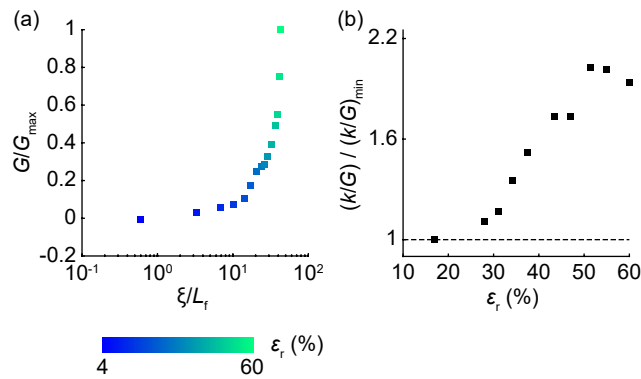


Figure S7. (a) The incremental shear modulus (G), normalized by the maximal modulus (G_{\max}), is governed by the level of permanent defects present (ξ), with $G > 0$ indicating stiffening. (b) Normalized ratio of incremental bulk stiffness (k) to incremental shear modulus (G) as a function of inclusion contraction levels prior to recovery (ϵ_r). The increase in k/G suggests that the encompassed matrix gradually becomes more constrained between inclusions, with k increasing more than G as the mechanical state becomes denser (Fig. 6a) and stiffer.

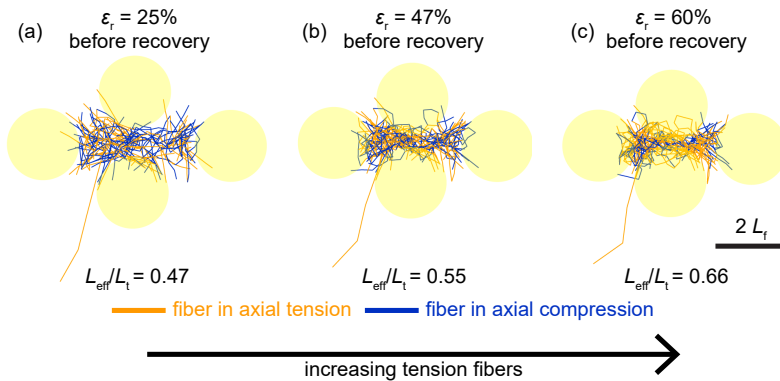


Figure S8. Another representative matrix between the recovered inclusions, showing fibers under axial tension (orange) and compression (blue). As inclusions underwent greater contraction prior to recovery, more tension fibers (orange) developed in the matrix, as seen from panels a to c.

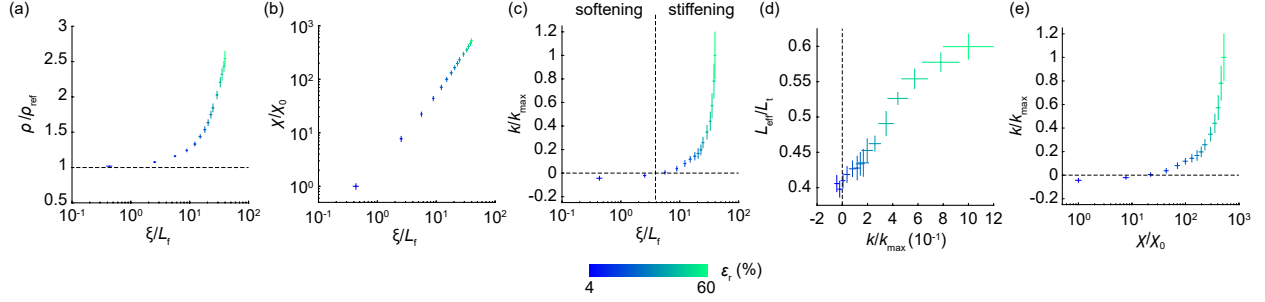


Figure S9. Data spread across means for the data points shown in Fig. 6a (panel a), Fig. 6b (panel b), Fig. 6c (panel c), Fig. 6g (panel d), and Fig. 6h (panel e). In all panels, error bars represent the standard error of the mean calculated from seven independent matrices. Color bar indicates inclusion contraction levels prior to recovery for the data points across all panels.

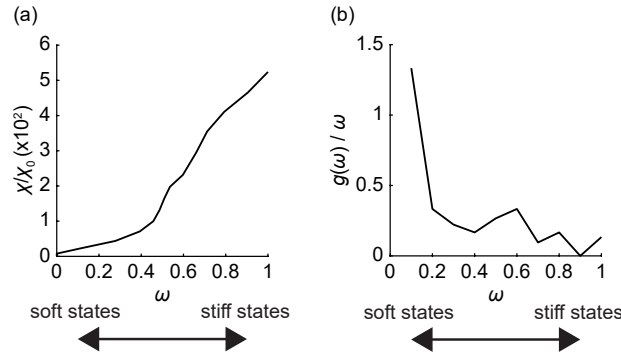


Figure S10. Heterogeneity and density of states. (a) Heterogeneity (χ) for different stable states (ω) of the encompassed matrix within the recovered cluster pursuant to their loading history. The states are defined as $\omega = \sqrt{k/\rho}$, where k and ρ represent the stiffness and physical fiber density of the respective states, respectively. (b) The reduced density of states, $g(\omega)/\omega$, exhibited a dominance of soft states (peak), suggesting a mechanical transition to a stiffening regime. See Supplemental Note 2 for details.

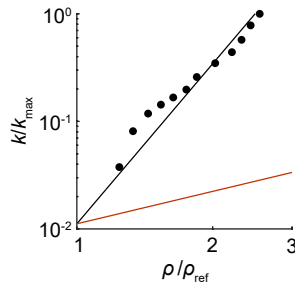


Figure S11. The normalized incremental bulk stiffness (k/k_{\max}) within the permanently deformed matrix region of interest inside the recovered cluster markedly surpasses the theoretical stiffness limit predicted by a linear relationship between normalized density (ρ/ρ_{ref}) and stiffness [3], depicted by the red solid line with a unit slope. Each data point represents the mean from seven independent matrices. On the log-log scale, the fitted black solid line indicates a power-law relationship: $k \propto \rho^n$, where $n = 4.9$ serves as the scaling factor. Looking ahead, this pronounced scaling driven by distorted fibers also exceeds the typical theoretical upper bound of 3 reported for other 2D micro-architected materials [4], including Ashby-Gibson cellular lattices. This opens exciting possibilities to leverage our stiffening mechanism in these systems, unlocking new directions for material design. However, the pronounced scaling observed in our 2D model is expected

to be somewhat reduced in 3D due to potential localization effects of defects [1] (see also Supplemental Fig. S15).

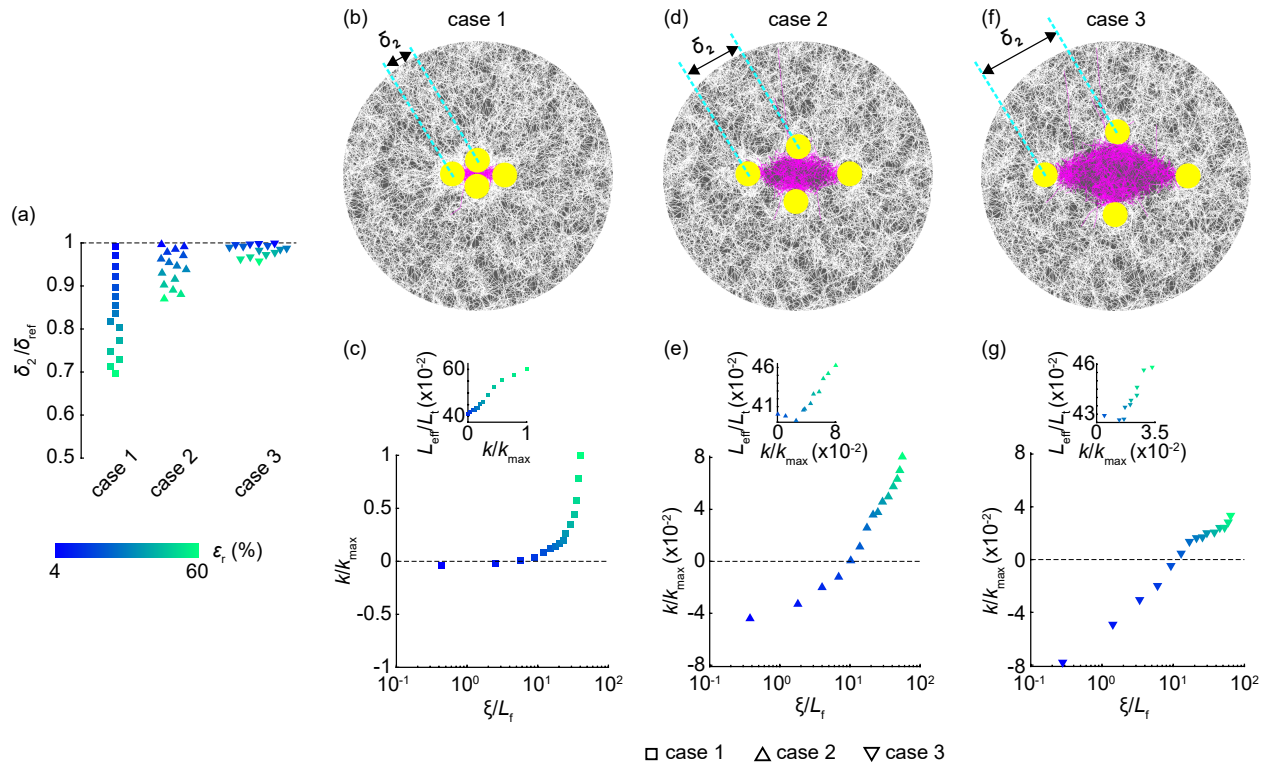


Figure S12. Effect of initial inter-inclusion spacing and size of the region of interest between inclusions. (a) Compared to case 1, greater initial spacings (δ_{ref}) in cases 2 and 3 result in less permanent reduction of inter-inclusion spacing (δ_2). (c–h) As permanent defects (ξ) accumulate, all cases eventually exhibit strain stiffening ($k > 0$). Insets: Whenever stiffening occurs, it is associated with the proportion of severely buckled fibers in tension (L_{eff}/L_t). k_{max} represents the maximal stiffness in case 1. Each data point in panels c, e, and h (including respective insets) represents the average from seven independent matrices. The color bar indicates the levels of inclusion contraction prior to recovery for the data points.

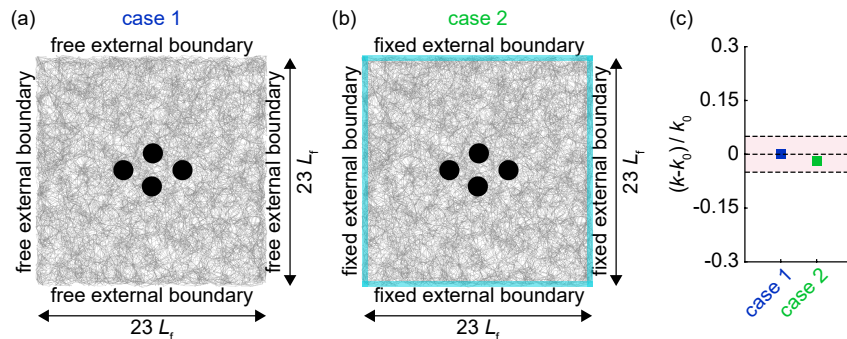


Figure S13. Consideration of free and fixed external boundaries. (a, b) Case 1 represents free external boundaries (panel a), while case 2 enforces fixed external boundaries, where matrix nodes at the edges (highlighted in blue) were constrained in both the x - and y -directions (panel b). Upon inclusion recovery¹,

¹Inclusions contracted by 60% before recovery.

the incremental bulk stiffness (k) of the encompassed matrix between inclusions was measured for both cases. (c) Constraining the external boundaries in case 2 introduced a negligible relative error ($\approx -1.9\%$) in stiffness compared to the reference case 1. k_0 is the reference stiffness that pertains to case 1. The pink-shaded region represents a $\pm 5\%$ relative error.

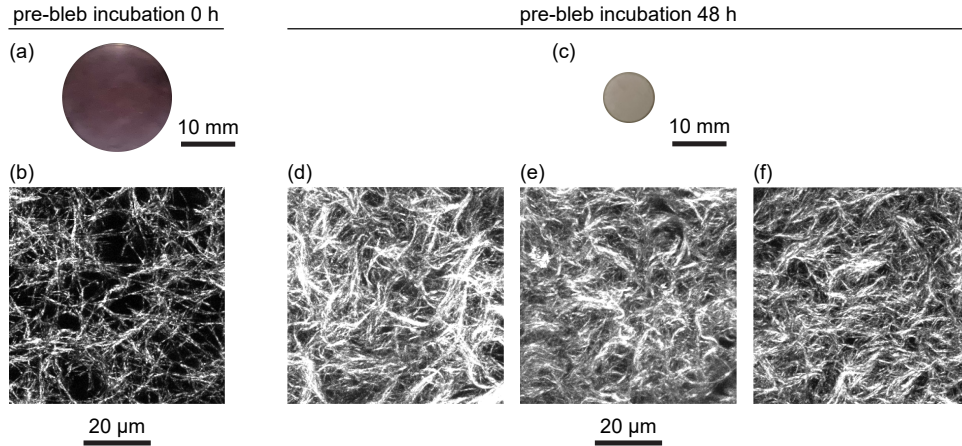


Figure S14. More representative confocal images of permanently deformed matrices. (a, b) For a cell-embedded matrix where cellular forces were inhibited immediately post-seeding using blebbistatin (panel a), a representative confocal image from a region of interest is shown in panel b. (c–f) Matrix after 48 h of cellular contraction prior to recovery by blebbistatin (panel c), with representative images from different regions of interest shown in panels d–f. Cells were 3T3.

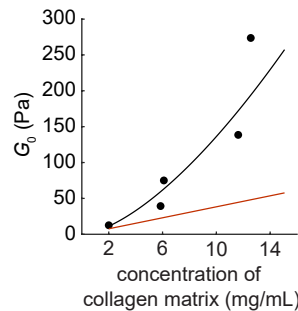


Figure S15. The shear modulus (G_0) of cell-embedded matrices (black dots), mechanically remodeled by the contraction and subsequent release of cell forces, exceeds the theoretical limit of modulus. This limit is traditionally predicted by a linear relationship between density (ρ) and modulus, as depicted by the red solid line with a unit slope. Each data point represents the average from at least four independent matrices embedded with different cell types (3T3 fibroblasts or myofibroblasts), each subjected to varying contraction durations before the release of cell forces. The fitted black solid line demonstrates a power-law relationship: $G_0 \propto \rho^n$, where $n = 1.55$ acts as the scaling factor.

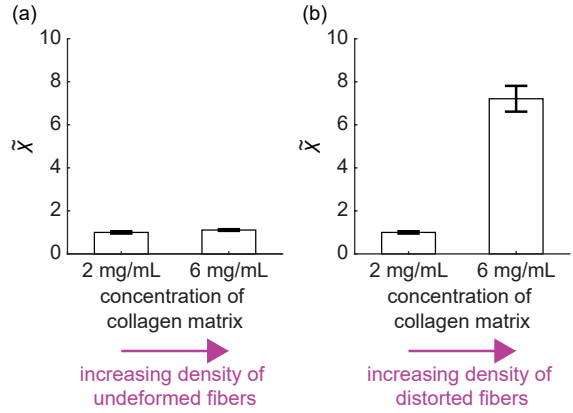


Figure S16. Sensitivity of the heterogeneity quantifier $\tilde{\chi}$ to the presence of distorted fibers in 3T3 cell-embedded collagen matrices. (a) We prepared collagen matrices at 2 and 6 mg/mL while inhibiting cell contraction via blebbistatin. Despite a $3\times$ increase in matrix density, $\tilde{\chi}$ remained unchanged, indicating that mere densification does not enhance matrix heterogeneity. (b) Allowing cells to contract for 24 h before cell force release by blebbistatin caused a permanent global contraction of the matrix, increasing both the overall fiber density by $3\times$ and the fraction of distorted (buckled and post-buckled) fibers. Under these conditions, $\tilde{\chi}$ rose significantly, demonstrating that fiber distortion, rather than densification alone, drives the increase in $\tilde{\chi}$. Each data point in panels a and b represents the mean and standard error of nine independent samples.

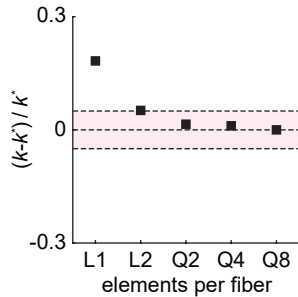


Figure S17. Mesh convergence study. Each fiber of the matrix was meshed using one linear beam element (L1), two linear beam elements (L2), two quadratic beam elements (Q2), four quadratic beam elements (Q4), and eight quadratic beam elements (Q8). The relative error in the incremental bulk stiffness (k) of the permanently remodeled matrix was evaluated within the dense cluster of four inclusions considered in this study² (Fig. 1b). The reference stiffness (k^*) was taken from the finest mesh (Q8) to calculate the relative error. Using two quadratic beam elements per fiber (Q2) provided a numerically efficient choice with a small relative error in stiffness ($\approx 1.5\%$). The pink-shaded region represents a $\pm 5\%$ relative error.

²Wherein cluster inclusions contracted 60% before recovery.

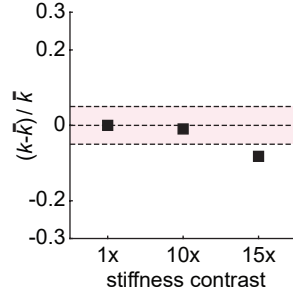


Figure S18. Avoidance of ill-conditioning. The stiffness contrast between the inclusions and matrix fibers was varied from $1\times$ to $10\times$ and $15\times$ to assess the relative error in the measured incremental bulk stiffness (k) of the permanently remodeled matrix within the dense cluster of four inclusions³. The reference stiffness (\bar{k}) was taken from the $1\times$ case. The pink-shaded region represents a $\pm 5\%$ relative error. Using a $10\times$ contrast in our study did not introduce bias in the stiffness measurement compared to the no-contrast scenario.

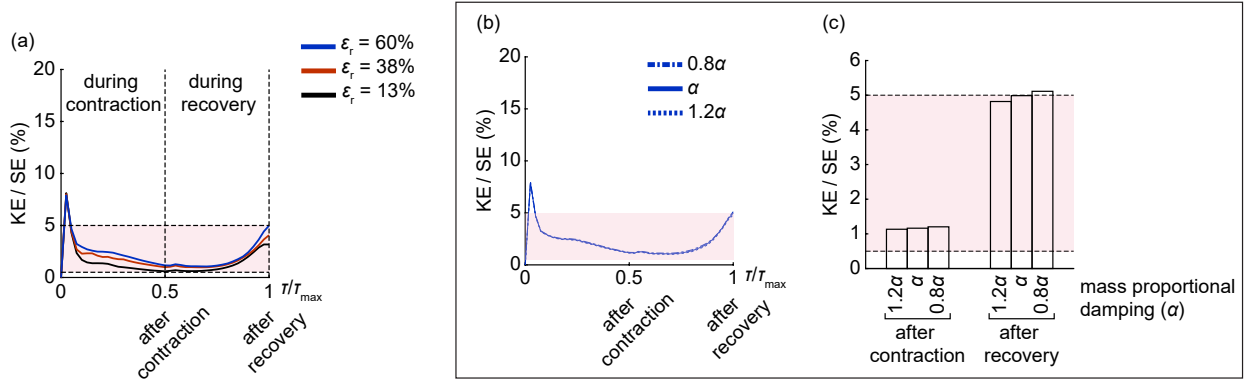


Figure S19. Numerical stability in implicit dynamic quasi-static solver. (a) Evolution of the kinetic-to-strain energy ratio (KE/SE) of the inclusion-matrix system (Fig. 1b) during inclusion contraction and recovery. The pink-shaded region indicates where the KE/SE ratio remained between $\approx 0.5\%$ and $\approx 5\%$, ensuring quasi-static conditions. Damping parameters were specified accordingly. See Supplemental Note 5 for further interpretation. Simulation time step (τ) was non-dimensionalized by the maximum time step (τ_{\max}). (b, c) The solver maintained stability under $\pm 20\%$ variation in the mass-proportional damping parameter (α) at a given mass density, as indicated by the gradual evolution of KE/SE with time steps. Panel c depicts KE/SE at the fully contracted and recovered states, respectively. Panels b and c refer to $\epsilon_r = 60\%$.

³Cluster inclusions contracted by 60% before recovery.

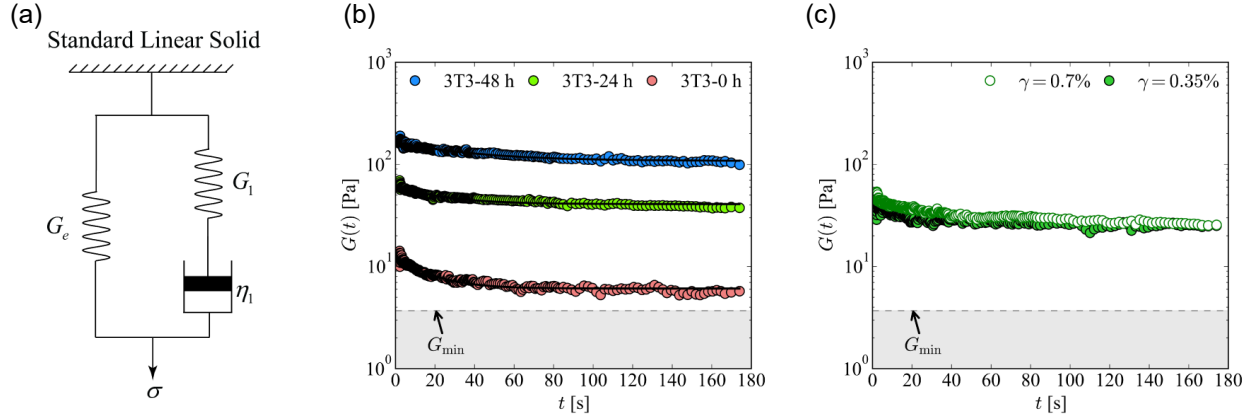


Figure S20. Measurement of the incremental modulus of a cell-embedded matrix using a rheometer. (a) The relaxation modulus $G(t)$ was measured after the cell-embedded matrix was probed with a low, step input shear strain $\gamma = 0.35\%$, and $G(t)$ was fitted to the standard linear solid model. Conceptually, the standard linear solid model comprises a purely elastic spring (modulus G_e) in parallel with a Maxwell element that includes a spring (modulus G_1) in series with a dashpot (viscosity η_1). In this model, the relaxation modulus $G(t)$ is given by $G(t) = G_e + G_1 e^{-t/\tau_1}$, where $\tau_1 = \eta_1/G_1$ is the relaxation time. (b) Representative relaxation moduli $G(t)$ at $\gamma = 0.35\%$ are shown for matrices remodeled by 3T3 cells that contracted for 24 h (green circles) and 48 h (blue circles) prior to recovery. The relaxation modulus $G(t)$ when 3T3 cells were not allowed to remodel the matrix is shown in red circles. Black solid lines represent the fits to the standard linear solid model. In the fitted model, the modulus value as $t \rightarrow 0$, denoted by $G_0 = G_e + G_1$, serves to indicate the incremental modulus of the matrix in each cell-remodeled state. For matrices with inert cells, G_0 indicates the incremental modulus of the matrix. For all matrices, G_0 remained above the minimum measurable shear modulus on the rheometer (noise floor), G_{\min} [5]. (c) The near overlap of the representative relaxation moduli $G(t)$ at $\gamma = 0.35\%$ and $\gamma = 0.70\%$ suggests that the incremental mechanical response at $\gamma = 0.35\%$ remained within the linear viscoelastic limits. This dataset pertains to a matrix remodeled by 3T3 cells over 24 h.

Supplemental Note 1: Evaluation of the microstructural gradient in fiber alignment surrounding the contracted cluster

To quantify the average extent of radial fiber alignment with the geometric center of the inclusion cluster relative to their reference orientation, we defined an order parameter S . We used this parameter to empirically depict the evolution of fiber alignment across three concentric regions surrounding the cluster, designated as regions I, II, and III (Supplemental Fig. S5a). These regions are defined by radial distances r from the cluster center, with S decreasing by more than 70% from region I to II and over 90% from region I to III. Region I (yellow), immediately surrounding the cluster, spans $r \approx 2.5L_f$ to $r \approx 5.5L_f$ from the cluster center. In contrast, Region III (grey), farther from the cluster, spans $r \approx 6L_f$ to $r \approx 11L_f$.

To capture spatial variations in fiber alignment, we calculated the spatial gradient of S , dS/dr . The magnitude of this gradient ($|dS/dr|$; Supplemental Fig. S5b) is interpreted as follows: it quantifies the sharp decrease in radial alignment of fibers moving outward in region I, captures the transition from high to low alignment in region II, and reflects the diminishing alignment at greater distances in region III. Notably, region I spans approximately $3L_f$ surrounding the cluster and exhibits a pronounced gradient, emphasizing its influence on the formation of permanent defects inside the cluster due to geometric confinement, as discussed in the Results section of the manuscript (Fig. 4).

Notably, in Fig. 7g of the manuscript, where we conducted a parametric study with sparser clusters, we

defined region I to span approximately $3L_f$ immediately surrounding the sparser clusters, where the gradient was prominent. This was done to maintain consistency with the spatial radial span of region I surrounding the denser cluster.

Supplemental Note 2: Geometric Randomness, Reduced Density of States and Mechanical Transition of the Matrix

The geometric randomness (or heterogeneity; χ) of the matrix between recovered inclusions represents the spectral energy of the displacement field, providing insight into how randomness influences mechanical states across different stable states (ω) (Supplemental Fig. S10a). Stiffer states are progressively shaped by increased structural randomness imparted by the recovering inclusions. At low ω , the system is dominated by soft states driven by buckled fibers. As ω increases, more buckled fibers transition into post-buckled configurations, and these distorted fibers induce geometric randomness, enhancing χ while also taking on tension, leading to an increase in matrix stiffness. Thus, the increase in $\chi(\omega)$ with ω reflects a disorder-driven mechanical transition in the matrix from soft to stiff states, where stiffer states are associated with higher geometric randomness.

The reduced density of states, $g(\omega)/\omega$, is another widely used metric that captures this transition by revealing how the distribution of mechanical states evolves with increasing ω (Supplemental Fig. S10b). In a 2D ordered system, $g(\omega)/\omega$ would remain constant according to Debye's theory. However, in our system, it exhibits a peak at low ω before decreasing as ω increases. This peak, a boson peak analog in disordered systems [6], corresponds to the abundance of buckling-dominated soft states in the matrix between recovered inclusions at low levels of ε_r . The presence of this peak is a hallmark of marginal stability in disordered materials near a mechanical transition, where an abundance of soft states exists [6]. In our system, this peak signifies that the matrix is on the verge of transitioning into a mechanically stiffening regime driven by densely packed distorted fibers, where the resulting stiff states are characterized by their heterogeneity (χ) and stiffness pursuant to the loading history of the matrix.

Together, these trends reinforce the argument of this manuscript that the mechanical response of the matrix has undergone a history-dependent transition from buckling-driven softening to postbuckling-driven stiffening.

Supplemental Note 3: Hamiltonian of the Encompassed Matrix Between Inclusions

The total strain energy stored in the matrix between inclusions evolves through contraction and recovery processes, with different energy storage mechanisms depending on the deformation state of the fibers. During contraction, fibers experience both axial tension and axial compression. Before buckling, fibers store both axial and bending strain energy, whereas after buckling, axial strain energy remains constant, and fibers gain only bending strain energy. The Hamiltonian after inclusion contraction is given by

$$\mathcal{H}_{\text{contract}} = \sum_i \int_0^{L_i} \left[\frac{1}{2}EA \left(\frac{\partial u}{\partial x} \right)^2 \Theta(\sigma_{\text{buckle}} - \sigma_i) + \frac{1}{2}EI \left(\frac{\partial^2 w}{\partial x^2} \right)^2 + \frac{1}{2}EA\varepsilon_{\text{buckle}}^2 \Theta(\sigma_i - \sigma_{\text{buckle}}) \right] dx. \quad (\text{Equation S1})$$

Here, the summation \sum_i runs over all fibers in the matrix, and L_i represents the length of the i -th fiber. The first term represents axial strain energy and applies only to fibers that have not yet buckled, as enforced by $\Theta(\sigma_{\text{buckle}} - \sigma_i)$. The second term represents bending strain energy, which is present in all fibers. The

third term ensures that axial strain energy in buckled fibers remains constant rather than increasing further after buckling, enforced by $\Theta(\sigma_i - \sigma_{\text{buckle}})$. Axial and transverse fiber deformations are depicted by u and w , respectively. E and A denote the fiber's Young's modulus and cross-sectional area, respectively.

During recovery, most fibers remain in axial compression, with the majority already buckled and accumulating bending strain energy. However, fibers that are still in axial compression but have not yet buckled continue to accumulate axial strain energy, and certain segments of postbuckled fibers experience confinement-induced axial tension, storing both axial and bending strain energy. The total strain energy after inclusion recovery is expressed as

$$\mathcal{H}_{\text{recover}} = \sum_i \int_0^{L_i} \left[\frac{1}{2}EA \left(\frac{\partial u}{\partial x} \right)^2 \Theta(\sigma_{\text{buckle}} - \sigma_i) + \frac{1}{2}EI \left(\frac{\partial^2 w}{\partial x^2} \right)^2 + \frac{1}{2}EA \varepsilon_{\text{buckle}}^2 \Theta(\sigma_i - \sigma_{\text{buckle}}) + \frac{1}{2}EA \left(\frac{\partial u}{\partial x} \right)^2 \Theta(p_{\text{conf}} - p_{\text{conf}}^*) \right] dx. \quad (\text{Equation S2})$$

As in the contracted state, the summation \sum_i runs over all fibers in the matrix, and L_i is the length of the i -th fiber. The first term represents axial strain energy stored in compressed fibers that have not yet buckled, as enforced by $\Theta(\sigma_{\text{buckle}} - \sigma_i)$. The second term represents bending strain energy, which is stored in all fibers. The third term accounts for axial strain energy that remains constant in buckled fibers. The fourth term accounts for axial strain energy stored only in confined postbuckled segments of fibers that are forced into tension due to geometric constraints, enforced by $\Theta(p_{\text{conf}} - p_{\text{conf}}^*)$. Typically, p_{conf} exceeds p_{conf}^* in a dense cluster (Fig. 7).

The emergence of axial strain energy in confined postbuckled fiber segments conceptually parallels the steric repulsion-driven fiber tension described in Ref. [7]. In both cases, an imposed spatial constraint redirects strain energy storage, leading to a mechanical transition in the matrix. While in Ref. [7], steric interactions between stiff inclusions stretch fibers into tension, in the present system, geometric confinement from recovered inclusions forces localized postbuckled fiber segments to take on tension (fourth term in Equation S2). In both cases, this emergent tension introduces a new mode of strain energy storage, contributing to a stiffening response in the fibrous matrix.

The emergence of axial tension in confined postbuckled fiber segments (fourth term in Equation S2) also parallels a prior observation [8] on geometrically confined postbuckled slender elastic beams, where confinement likely drives a redistribution of strain energy into axial modes.

Shear strain energy in fiber segments was negligible throughout the contraction and recovery of inclusions due to their sufficient slenderness.

Supplementary Note 4: Justification for Using an Implicit Solver, Limitations and Considerations for Future Improvement

This study involved simulating the contraction and recovery of a cluster of four closely spaced inclusions embedded in a fibrous matrix using an implicit dynamic quasi-static solver in Abaqus/Standard. The solver accounted for large deformations and mechanical instabilities, particularly fiber buckling, occurring during the contraction and recovery processes. Given the instability-prone nature of the system, selecting an appropriate solver was crucial to maintaining numerical stability while preserving physically relevant buckling events. An implicit dynamic solver was chosen over an explicit solver due to its ability to efficiently enforce quasi-static conditions while handling large deformations without requiring excessively small time

steps. However, for future studies involving larger inclusion clusters, where the number of instability-driven events increases, an explicit solver may offer advantages in resolving rapid microstructural changes.

Following our prior work on inclusion-matrix systems [1, 9], the implicit solver was preferred in this study because it naturally enforces equilibrium at each time step, ensuring that kinetic energy remains a small fraction of strain energy (see Supplemental Note 5). This avoids the need for artificial stabilization techniques, such as mass scaling, required in explicit solvers to achieve a quasi-static response. Additionally, implicit solvers are unconditionally stable, allowing for relatively larger time steps compared to explicit solvers, making them computationally efficient for our quasi-static problem. The adaptive time-stepping capability of the implicit solver helped control time steps based on the evolution of instabilities, applying artificial damping when necessary to suppress excessive kinetic energy growth while still permitting buckling-driven transitions. Unlike explicit solvers, which require very small time steps to maintain stability, the implicit solver efficiently handled large deformations without excessive computational cost.

While the implicit solver performed well for the four-inclusion system, increasing the number of inclusions presents additional challenges. A larger number of inclusions recovering simultaneously leads to increased kinetic energy fluctuations, making it more difficult to prevent kinetic-to-strain energy ratios (KE/SE) from exceeding acceptable quasi-static limits. The iterative nature of the implicit solver also struggles to converge when multiple inclusions recover simultaneously. As seen in the four-inclusion case, kinetic energy increased up to $\approx 5\%$ of the strain energy during recovery (Supplemental Fig. S19). With a larger number of inclusions, this effect is expected to be more pronounced, potentially causing the system to deviate from a quasi-static regime.

For simulations involving significantly larger inclusion clusters, an explicit solver may offer some advantages. Since explicit solvers update displacements directly without requiring iterative convergence, they are well-suited for simulating the recovering inclusion problem with a rapid increase in mechanical instabilities. They also do not require equilibrium iterations at each time step, reducing the risk of non-convergence. Explicit solvers use very small time steps, allowing them to resolve rapid kinetic energy fluctuations without requiring artificial damping.

However, explicit solvers also have notable drawbacks. Because they rely on conditionally stable time steps, they require significantly smaller time steps than implicit solvers, making them computationally expensive for quasi-static simulations. To reduce computational cost, explicit solvers require mass scaling, which can introduce artificial inertial effects that alter the physics of the system. Moreover, since explicit solvers are inherently dynamic, maintaining a quasi-static response requires careful tuning of time steps and damping strategies.

For the current study, the implicit solver was the best choice as it effectively handled the contraction and recovery of four closely spaced inclusions while maintaining a quasi-static response without excessive computational cost. This provided a minimal model to understand the mechanics of the matrix enclosed by the inclusion cluster. For future studies with larger inclusion clusters, an explicit solver may be advantageous due to its ability to resolve a large number of instabilities.

Supplementary Note 5: Numerical Stabilization in an Implicit Dynamic Quasi-Static Solver During the Contraction and Recovery of Inclusions

Our simulations involved a cluster of four closely spaced inclusions embedded in a fibrous matrix, which contracted during the first load step and recovered during the second load step. An implicit dynamic quasi-static solver in Abaqus/Standard was used with the nonlinear geometry option enabled to account for large deformations and mechanical instabilities arising from fiber buckling during the contraction and re-

covery of the inclusions. Given the instability-prone nature of the system, an initial prescription of damping was required to ensure numerical stability and convergence without suppressing physically relevant fiber buckling events. By incorporating this controlled level of damping through an initial assignment of the mass-proportional damping parameter α and mass density, the simulation effectively mitigated excessive oscillations while preserving physically meaningful instability-driven deformations (e.g., long range displacement propagation in the matrix aided by buckled fibers).

To accurately capture buckling instabilities, a slightly underdamped system was used rather than an overdamped one. This approach allowed real instability-driven events to occur naturally, avoiding excessive smoothing that could artificially restrict the bending and buckling of fibers due to excessive damping.

During the inclusion contraction process, the ratio of kinetic energy (KE) to strain energy (SE) in the model (KE/SE) initially exhibited oscillations due to underdamping but gradually decreased below 5% as contraction progressed (Supplemental Fig. S19a). Adaptive time-stepping in the implicit dynamic solver was used to adjust the time step size in response to the level of instabilities produced. The adaptive solver applied artificial damping by dynamically reducing the time step size, preventing excessive KE growth while allowing instability-driven events to be accurately captured. As a result, KE/SE progressively decreased throughout inclusion contraction, stabilizing at approximately 1% at full contraction, confirming that the system maintained its quasi-static nature. To ascertain that adaptive time-stepping did not introduce excessive artificial damping, we prescribed a minimum time increment threshold in the adaptive time-stepping scheme, ensuring that KE/SE never dropped below $\approx 0.5\%$ for all inclusion contraction levels studied. This approach effectively negated the possibility of artificial (non-physical) viscoelastic effects.

During the recovery of inclusions, while SE gradually decreased, additional buckling events occurred, leading to a gradual increase in KE/SE up to $\approx 5\%$. This increase in KE/SE resulted from the competition between new instability-driven oscillations, which introduced kinetic energy, and adaptive damping from the solver's time-stepping scheme, which suppressed excessive KE growth to maintain numerical stability and preserve the quasi-static nature of the problem.

This discussion suggests that solving the recovery process posed a greater challenge. Given the reliance on fiber buckling, it was necessary to keep the system slightly underdamped at the beginning to avoid masking buckling events within the cluster during inclusion contraction. However, the recovery process was prone to generating additional buckling-driven oscillations, which, when coupled with the decreasing strain energy, tended to drive KE/SE upward. Our chosen damping parameters (α and mass density) maintained KE suppression during recovery for the four-inclusion problem. While the choice of α governs the evolution of KE/SE, its effect remains relatively stable, showing minimal sensitivity to variations within a $\pm 20\%$ range of α (Supplemental Fig. S19b,c). Although a low mass density was chosen, it did not cause ill-conditioning, as evidenced by the smooth evolution of KE/SE.

However, introducing a larger cluster of more than four inclusions presents additional challenges, as it would generate even more instabilities during recovery, making it increasingly difficult to prevent KE/SE from becoming excessively large, causing the system to deviate from a quasi-static regime. A more dedicated future study should address this challenge for larger inclusion clusters, ensuring that physically relevant buckling events are not suppressed during inclusion contraction while also preventing KE/SE from growing uncontrollably during inclusion recovery.

Supplemental Note 6: Equations of parameters in numerical simulations

Definition of S

$$S = \left(\frac{S_{\text{def}}}{S_{\text{ref}}} - 1 \right) \times 100, \quad (\text{Equation S3})$$

where,

$$S_{\text{def}} = \frac{1}{N} \sum_{i=1}^N |\cos(\theta_i^{\text{def}})|, \quad S_{\text{ref}} = \frac{1}{N} \sum_{i=1}^N |\cos(\theta_i^{\text{ref}})|,$$

where N is the total number of fibers in the regions of interest surrounding the cluster (regions I, II, and III in Supplemental Fig. S5), and θ_i^{def} and θ_i^{ref} are the angles between the i -th fiber's tangent vector and the outward radial vector from the cluster center to the center of the i -th fiber in the deformed and reference states of the matrix, respectively.

Definition of χ

The heterogeneity parameter χ quantifies the total spectral energy of the permanent nodal displacement field \mathbf{u} within the region of interest inside the recovered cluster (e.g., Fig. 3d). It is calculated by summing the power across all frequency components of the Discrete Fourier Transform (DFT) of \mathbf{u} , $\hat{\mathbf{u}}(\tilde{k})$, where \tilde{k} represents the wave numbers. The power of each frequency component is computed by normalizing the squared magnitude of the DFT coefficients by the number of frequency bins, n . The equation for χ can be expressed as follows:

$$\chi = \sum_{\tilde{k}=1}^n \frac{|\hat{\mathbf{u}}(\tilde{k})|^2}{n} \quad (\text{Equation S4})$$

This formulation provides a comprehensive measure of the total energy distributed across the frequency spectrum, indicating the level of heterogeneity or randomness in the permanent displacement field due to distorted (buckled or post-buckled) fibers in the matrix.

Definition of k

$$k = \frac{\partial^2 W}{\partial \xi^2} \quad (\text{Equation S5})$$

where, W represents the total strain energy of the fibers in the region of interest within the matrix. ξ denotes the internal variable representing the total length of defects (total excess lengths) in the fibers within the same region of interest.

Supplemental Note 7: Definition of $\tilde{\chi}$ in cell-embedded collagen matrices

The heterogeneity quantifier $\tilde{\chi}$ measures the total spectral energy of the intensity field within a matrix, reflecting its permanently remodeled state after cell contraction and recovery. This is quantified by subdividing each image into subsets (32×32 pixels or $6.6 \times 6.6 \mu\text{m}^2$), computing the Fourier transform of pixel intensities within each subset, and summing the power across all frequency components. Let $\hat{I}(\tilde{k})$ represent the Discrete Fourier Transform (DFT) coefficients for the pixel intensities, where \tilde{k} is the wave number. The

power of each frequency component is normalized by the total number of frequency bins, n . The equation for $\tilde{\chi}$, averaged over all subsets in the representative image, is given by:

$$\tilde{\chi} = \frac{1}{M} \sum_{i=1}^M \left(\sum_{\bar{k}=1}^n \frac{|\hat{I}_i(\bar{k})|^2}{n} \right) \quad (\text{Equation S6})$$

Here, M represents the total number of subsets analyzed per image, and n is the total number of frequency bins used in the DFT. This method aggregates the spectral energy across the entire frequency spectrum, thereby providing a quantitative measure of the geometric heterogeneity of the matrix.

References

- [1] M. Sarkar, B. M. Burkel, S. M. Ponik, J. Notbohm, Unexpected softening of a fibrous matrix by contracting inclusions, *Acta Biomater* 177 (2024) 253–264.
- [2] A. Zakharov, M. Awan, A. Gopinath, S.-J. J. Lee, A. K. Ramasubramanian, K. Dasbiswas, Clots reveal anomalous elastic behavior of fiber networks, *Sci Adv* 10 (2) (2024) eadh1265.
- [3] M. A. Meyers, K. K. Chawla, *Mechanical behavior of materials*, Cambridge university press, 2008.
- [4] N. A. Fleck, V. S. Deshpande, M. F. Ashby, Micro-architected materials: past, present and future, *P Roy Soc A-Math Phys* 466 (2121) (2010) 2495–2516.
- [5] R. H. Ewoldt, M. T. Johnston, L. M. Caretta, *Experimental Challenges of Shear Rheology: How to Avoid Bad Data*, Springer New York, New York, NY, 2015, Ch. 6, pp. 207–241.
- [6] Y.-C. Hu, H. Tanaka, Origin of the boson peak in amorphous solids, *Nat Phys* 18 (6) (2022) 669–677.
- [7] J. L. Shivers, J. Feng, A. S. van Oosten, H. Levine, P. A. Janmey, F. C. MacKintosh, Compression stiffening of fibrous networks with stiff inclusions, *P Natl Acad Sci USA* 117 (35) (2020) 21037–21044.
- [8] J. Miller, T. Su, J. Pabon, N. Wicks, K. Bertoldi, P. M. Reis, Buckling of a thin elastic rod inside a horizontal cylindrical constraint, *Extreme Mech Lett* 3 (2015) 36–44.
- [9] M. Proestaki, B. Burkel, E. E. Galles, S. M. Ponik, J. Notbohm, Effect of matrix heterogeneity on cell mechanosensing, *Soft Matter* 17 (2021) 10263–10273.